CHARACTERIZATION AND VERIFICATION OF THE RITA PAYLOAD HYPERSPECTRAL IMAGER IN ALAINSAT-1, AS PART OF THE 2ND IEEE GRSS STUDENT GRAND CHALLENGE

L. Contreras-Benito [1,2], A. Gonga [1,2], I. Crisan [1], A. Perez-Portero [1,2], A. Garcia [1], G. Gracia-Sola [1], J. Ramos-Castro [2,3], A.H. Jallad [4], A. Camps [1,2,5]

[1] CommSensLab – UPC, Dept. of Signal Theory and Communications, UPC – BarcelonaTech, E-08034 Barcelona, Spain
[2] Institute of Space Studies of Catalonia (IEEC) – CTE-UPC, E-08034 Barcelona, Spain.
[3] Dept. of Electronic Engineering, UPC – BarcelonaTech, E-08034 Barcelona, Spain
[4] National Space Science and Technology Center, UAE University, CoE, POBox 15551 Al-Ain, UAE
[5] ASPIRE Visiting International Professor, UAE University, CoE, POBox 15551 Al-Ain, UAE

ABSTRACT

The Remote sensing and Interference detector with radiometry and vegetation Analysis (RITA Payload) [1] is a development of the UPC NanoSat Lab, aimed at Earth Observation (EO). It is one of the winners of the Second IEEE GRSS Student Grand Challenge, and will fly on-board AlainSat-1, a 3U CubeSat developed by the National Space Science and Technology Center (NSSTC) of the United Arab Emirates.

RITA hosts three experiments. An L-band microwave radiometer (MWR) will gather data of soil moisture and sea ice thickness and concentration, aided with a Radio-frequency Interference (RFI) detection algorithm. A LoRa transceiver will perform on-demand execution of the EO experiments[2]. Finally, a Near-Infrared (NIR) Hyperspectral Camera will gather data for vegetation monitoring, agriculture applications, hydrology and coastal and inland waters mapping, among others [3].

This work is focused on the calibration and validation of the Hyperspectral imager, at optical, electronic and spectral levels, as well as in the verification of its performance to measure Normalized Difference Vegetation Index (NDVI).

Index Terms— CubeSat, Hyperspectral Camera, Earth Observation, Educational.

1. INTRODUCTION

During recent years, desertification and flood events are becoming more frequent due to climate change. In order to study their evolution, measurements of the so-called Essential Climate Variables (ECVs) need to be acquired with sufficient accuracy to be properly analysed, such as soil moisture, ocean surface salinity and vegetation density and health, etc. Hyperspectral images, specially near-infrared (NIR) sensors, are commonly used to acquire high resolution vegetation measurements, but the large size of the lenses and elevated cost makes it difficult to integrate in small platforms. RITA will demonstrate the ability of integrating these COTS imagers in a single compact, fitting in a single CubeSat unit

To properly guarantee the quality of the measurements, the instruments must be properly calibrated [4]. A comprehensive set of tests have been performed, both at ambient conditions, and in a space-like environment (Thermal Vacuum Chamber, TVAC). The results of the calibration and validation campaign will be used to properly integrate the systems in the payload and as corrections of the in-orbit acquired data.

1.1. System Description

The Hyperspecral Camera is the PhotonFocus MV1 D2048-1088 96-G2[5]. It uses the CMOS CMV2K-SM5x5-NIR sensor from IMEC, with a resolution of 2048×1088 pixels, and a snapshot mosaic array of 25 Fabry-Pérot-type filters. The camera's spectral range goes from 600 to 975 nm. The optical element is a Kowa LM16HC-V 16 mm fixed focal lens, along with a SP850-HT short-pass filter (SPF) and a LP645 long-pass filter (LPF), with respective cut-off wavelengths at 850 nm and 645 nm. The lens and the camera are fixed to a custom mount with an integrated baffle to reduce stray light on the sensor. The payload's main processor is an Analog Devices ADRV9364.

One of the main products will be the Normalized Difference Vegetation Index (NDVI), to assess the status of the vegetation, which will also be used for pixel down-scaling algorithms. As this parameter is obtained by comparing the red band with the infrared region, the spectral response of the imager must be calibrated. The longer wavelength bands were found to have additional secondary responses in the upper-red part of the spectrum, thus interfering with the NDVI calculations. The long-pass filter was introduced to mitigate this effect.

The system is completed with the RF Front-End board, which includes a LoRa and S-Band communications systems and a MWR chain. On the outer part of the CubeSat, a dielectric substrate contains the three patch elements of the MWR antenna and the LoRa patch antenna.

Fig. 1: RITA Payload module system components.

2. METHODOLOGY

Through the verification campaign, several tests were performed to study the characteristics of the camera under different environmental conditions. The imager pixels provide a Quantified Brightness expressed as a Digital Number (DN) between 0 and 65535 ($2^{16} - 1$).

2.1. Brightness Linearity

Brightness linearity tests were carried out to measure the response of the sensor against an illuminated target for different exposure times. The response of the system is expected to be linear up to a certain saturation level. The central Region of Interest (ROI) of the images are used in the calculations to minimize the effects of the uneven illumination of the target. The mean DN of a central ROI 10% of the total image size is computed for the different exposure times, as well as the relative error from a perfect linear output.

2.2. Depth of Field and Field of View

The employed lens has a focal length of $f = 16$ mm, and the hyperfocal distance of the lens-sensor system will be determined for a 550 km LEO orbit. For a fixed focal length, the Depth of Field (DoF, Eq. 1) depends on the distance to the object x and the optical aperture N, being $N = 1.4$ the maximum of this lens. In addition, the Circle of Confusion C describes the non-ideallity of the focal point.

$$\mathrm{DoF} = \frac{2x^2 \cdot N \cdot C}{f^2} \tag{1}$$

A checkered pattern target with 5 mm sided squares is used to take calibration pictures from different distances. A ROI located at the separation of two columns of squares is studied to compute the transition width W (in pixels) between consecutive squares (Fig. 2), via a fitted sigmoid curve. The best focus is assigned to the least W row of pixels, and the allowable blur is defined as $2 \times W_{min}$. The DoF is then set as the number of pixel rows (in mm) within the allowable blur.

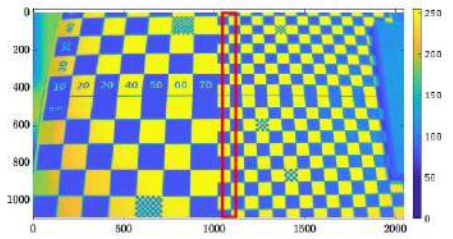

Fig. 2: Checkered Target tilted at 30° and ROI (red area).

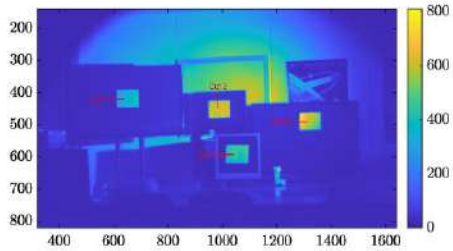

Fig. 3: Integrated DN difference between ambient and 45 °C.

The target will be angled 30° and 60° to calculate the DoF at different conditions. Once the DoF is known, C can be obtained and the hyperfocal distance H can be calculated:

$$H = \frac{f^2}{N \cdot C} + f \tag{2}$$

From the non-tilted images, the pixel size is computed, and from them, the lateral size of the image h_i is obtained. The Field of View (FOV) can be calculated for the horizontal and vertical angles by geometric relation.

2.3. Blur under environmental stress

The payload will undergo thermal cycling during orbital operations, which leads to thermal contraction and expansion of the parts. This may cause blurring of the images, reducing their scientific quality. Several tests are performed in the TVAC varying from 5°C to 45°C.

A set of high contrast targets are placed outside of the TVAC at the hyperfocal distance (Fig. 3). The difference between ambient images ($25°C$, 1 atm) and the rest is integrated over all the pixels. A sigmoid is then fitted to the dark to bright transition of the targets, as in Section 2.2. For each cut, the Relative Standard Deviation of all the sigmoids is calculated (considering all the thermal cycles) and then averaged.

2.4. Dark Current and Fixed Pattern Noise

Dark current appears in photosensitive elements produced mostly by thermal excitation or semiconductor defects [6]. It

depends on the temperature and exposure time. The dark current measurements were performed inside the TVAC. Images were taken to quantify the noise floor and the temperature and exposure time correlation. The DN readings are transformed to Dark Current (in e^-) from the manufacturer's Full Well Capacity. A linear fit is applied to the exposure time evolution, and an Arrhenius exponential fit to the temperature variation. The dark images taken will be used to subtract the Fixed Pattern Noise (FPN) from the in-orbit images.

2.5. Defective Pixels

Defective pixels yield values significantly different from neighbouring pixels under same conditions. Five images are averaged at 4 different exposure times, with the camera pointing towards an evenly illuminated surface. The lens is not installed to guarantee homogeneous illumination. The defective pixels are then detected by means of the algorithm presented in [7]. For this test, noise is assumed to be Gaussian shaped, and a threshold is set to separate the noise from the actual defective measures. If a pixel has a defective behaviour in 3 or 4 of the different exposures, it is considered as defective and is subtracted from the scientific images.

2.6. Optical Vignetting

Optical vignetting is the brightness reduction at the edges of an image arising from the difference of the light rays crossing the lens at different relative inclination with respect to the optical axis. Images are taken of an illuminated white wall. To compensate for the uneven lightning, lateral auxiliary images are taken with increasing distance to the light source.The central ROI is averaged to estimate the lightning degradation of the surface. This effect is then subtracted from the actual images to separate it from the vignetting.

2.7. Spectral Response Caracterization

The exact spectral response of each band is obtained using a calibrated monochromator at the CD6-UPC facilities. The transmittance of the lens is fitted to a Rayleigh type distribution from the manufacturer data. The temperature effects on the sensor, monochromator response, fixed-pattern noise and exposure time are considered for processing the images. The LPF will limit the appearance of the secondary response on the longer wavelength channels. A sweep from 400 to 1000 nm is performed in steps of 3 nm with the monochromator.

The characterization of the camera is concluded gathering images of areas with mixed vegetation and buildings to validate the usefulness of the image to generate NDVI maps. The NDVI is calculated for every macro-pixel j as in Eq. 3[8]. Note that the DN values are already calibrated.

$$NDVI_j = \frac{DN^{Cal}_{NIR,j} - DN^{Cal}_{Red,j}}{DN^{Cal}_{NIR,j} + DN^{Cal}_{Red,j}} \quad (3)$$

3. RESULTS

Brightness Linearity: From the images acquired at different exposure times, a linear fit is adjusted to the average DN of the central ROI. The deviation from a perfect line is also calculated. The maximum deviation is 0.36%, with a Linearity Error of 0.34%.

Field of View and Depth of Field: It is found that Horizontal FoV is $\mathrm{HFoV} = 39.0 \ \pm 1.2°$, and the Vertical is $\mathrm{VFoV} = 20.7 \ \pm 0.6°$. This is compliant with the requirement that the HFoV must be $\pm 5°$ of the MWR footprint, which is $40°$.

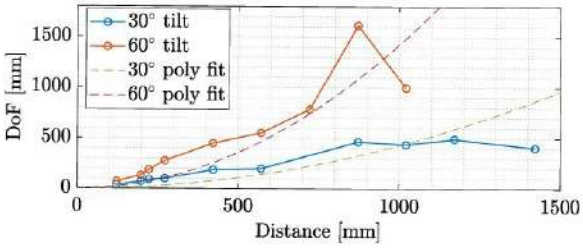

Fig. 4: DoF as a function of the distance and tilt angle.

The DoF is calculated for different distances and $30°$ and $60°$ tilt angles. A positive non-translated parabola is fitted to the results (Fig. 4). With Eq. 1, C_{30} and C_{60} are obtained. From Eq. 2, the hyperfocals $\boldsymbol{H_{30} = 6.44\ \mathrm{m}}$ and $\boldsymbol{H_{60} = 1.41\ \mathrm{m}}$ are calculated. As it is expected that the in-orbit images will be taken almost with Nadir Pointing, H_{30} is taken as the lower bound for setting the lens focus.

Thermal Cycling Blur: After an initial increase in the absolute integrated difference from images in ambient and vacuum, the shots do not present an accumulated difference during thermal cycling, returning to the initial conditions after the test. The mean Relative Standard Deviation of all the transition of the cuts is 3.89%, corresponding to a width of 3 pixels.

Dark Current: The dark current behaviour in front of the exposure time is found to be linear for each set of cases between $5°$C and $45°$C, as expected. With the results of each case, the temperature dependence is found to follow the Arrhenius law (Fig. 5).

Defective Pixels: One pixel was found defective more than two times, being detected on the four experiments. The rest of the pixels detected in one or two are considered as being affected by noise.

Optical Vignetting: After compensating for the wall light degradation pattern, the expected parabolic behaviour of the optical vignetting was obtained, as shown in Fig. 6.

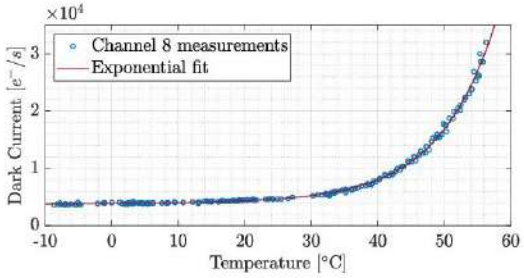

Fig. 5: Mean Dark Current temperature relation.

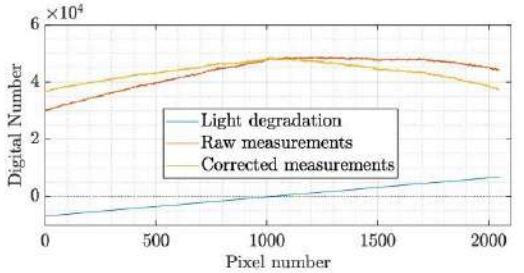

Fig. 6: Corrected optical vignetting behaviour.

Spectral Response: The measured response of each band corresponds to the expected behaviour. In addition, the effect of the LPF is validated, eliminating the secondary responses of the bands (Fig. 8). The NDVI validation yielded satisfactory results, highlighting vegetation in front of buildings (Fig. 7).

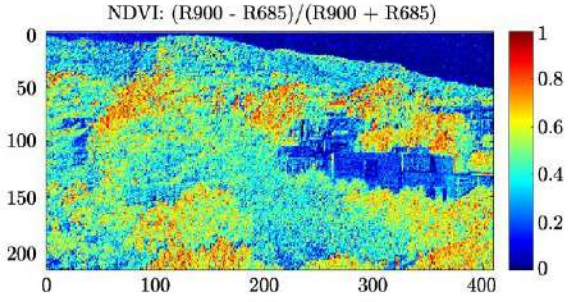

Fig. 7: Sample NDVI of a target area in Barcelona.

4. CONCLUSIONS

An exhaustive test campaign was conducted to ensure the quality of the mission data. The optical, electronic and spectral parameters of the different components were characterised, as well as the response of the whole system, and the system requirements were validated. The results of the characterization campaign have been used to integrate the camera and prepare the payload for flight, and they will be considered in the processing of the final in-orbit images.

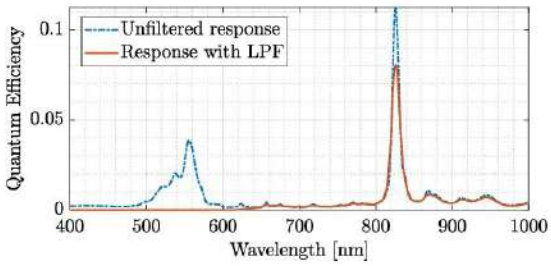

Fig. 8: Filtered and unfiltered response of Channel 23.

Acknowledgements

This project is supported and funded by the IEEE Geoscience and Remote Sensing Society (GRSS), as one of the winners of the 2nd IEEE GRSS Student Grand Challenge. It is also part of the project "GENESIS: GNSS Environmental and Societal Missions – Subproject UPC", Grant PID2021-126436OB-C21 funded by the Ministerio de Ciencia e Investigación (MCIN) / Agencia Estatal de Investigación (AEI) / 10.13039/501100011033 and EU FEDER "Una manera de hacer Europa". We would finally like to thank Metitxell Vilaseca and the Centre for Sensors, Instruments and Systems Development (CD6) of the UPC for their help and the use of the facilities for the camera characterization.

5. REFERENCES

[1] A. Perez-Portero et al., "RITA: A 1U multi-sensor payload for the GRSSSAT contributing soil moisture, vegetation analysis and RFI detection," in *2021 IEEE International Geoscience and Remote Sensing Symposium IGARSS*, 2021.

[2] L. Fernandez et al., "On-demand satellite payload execution strategy for natural disasters monitoring using LoRa: Observation requirements and optimum medium access layer mechanisms," *Remote Sensing*, vol. 13, no. 19, pp. 4014, Oct. 2021.

[3] M. Rast and T. H. Painter, "Earth observation imaging spectroscopy for terrestrial systems: An overview of its history, techniques, and applications of its missions," *Surveys in Geophysics*, vol. 40, no. 3, Mar. 2019.

[4] E. de Miguel et al., "Caracterización del sensor aeroportado CFL del INTA," in *XIX Congreso de la Asociación Española de Teledetección*, 2022, pp. 429–432.

[5] PhotonFocus, "Industrial camera MV1-D2048x1088-96-G2," `https://www.photonfocus.com/products/camerafinder/camera/mv1-d2048x1088-96-g2/` [Last visited January12th, 2023].

[6] A. Rogalski et al., "Infrared detector characterization," in *Antimonide-based Infrared Detectors*. SPIE, 2018.

[7] A.D. Restrepo and H. Loaiza-Correa, "A new algorithm for detecting and correcting bad pixels in infrared images," *Ingenieria e Investigacion*, vol. 30, no. 2, pp. 197–207, May 2010.

[8] F. Khoirunnisa, Supriatna, and A. Wibowo, "Using NDVI algorithm in Sentinel-2A imagery for rice productivity estimation," *IOP Conference Series: Earth and Environmental Science*, vol. 481, no. 1, pp. 012064, Mar. 2020.